ELSEVIER

Journal of Nuclear Materials 273 (1999) 192–202

journal of nuclear materials

www.elsevier.nl/locate/jnucmat

Fatigue failure analysis of V–4Ti–4Cr alloy

H. Aglan [a,*], Y.X. Gan [a], B. Chin [b], M. Grossbeck [c]

[a] *Mechanical Engineering Department, Tuskegee University, Tuskegee, AL 36088, USA*
[b] *Center for Materials Research and Education, Auburn University, Auburn, AL 36849, USA*
[c] *Oak Ridge National Laboratory, Oak Ridge, Tennessee, USA*

Received 27 October 1998; accepted 11 January 1999

Abstract

In the present work, the fatigue fracture and failure behavior of a V–4Ti–4Cr has been studied. Static tests were conducted to study the overloading behavior and to select the magnitude of the stress level for the fatigue studies. Fatigue tests were performed using single edge notched (SEN) specimens under tension–tension load control conditions. Fatigue crack propagation (FCP) data such as the crack length, number of cycles, and hysteresis loops were recorded to calculate the crack speed, the energy release rate, and the change in work expended on damage formation and dissipative processes within the material. Parameters characterizing the fatigue fracture resistance of V–4Ti–4Cr alloy, namely the specific energy of damage (γ'), and the dissipative coefficient (β'), were determined from the fatigue data using the modified crack layer (MCL) theory. Fracture surface examination using scanning electron microscopy (SEM) revealed ductile failure mechanisms under tensile overloading conditions. The fatigue fracture surface of the V–4Ti–4Cr consists of three distinct regions, corresponding to the threshold, stable and unstable crack propagation stages.

1. Introduction

Modern fusion reactors require novel metallic alloys with many diverse combinations of properties such as resistance to severe radiation, chemical inertness in liquid metal systems, good thermal conductivity, and superior high temperature strength. Various metals and alloys have been considered as fusion reactor first wall and blanket materials. These include tungsten, tantalum, niobium, zirconium, titanium, molybdenum, tantalum-coated nickel, chromium, nickel, stainless steel, Nimonic™, Inconel™, and vanadium [1]. Among all the above materials, vanadium alloy exhibits many favorable characteristics for fusion reactor applications. Vanadium is a hard, silvery-white metal and has a body-centered cubic structure [2]. The melting point of vanadium is above 1700°C [3]. Vanadium alloys are believed to provide significant advantages in high temperature applications due to their high surface heat flux, superior neutronic properties, potentially better radiation damage resistance, and superior corrosion resistance in liquid alloys [4]. Studies on the corrosion of vanadium by liquid metals have been performed. High resistance to attack by various liquid metals, such as sodium, lithium, Li–Pb alloy, Bi–Pb alloy and Bi–In–Sn ternary alloy systems, have been reported [5].

Recent research on vanadium and vanadium alloys has been focused on the following aspects: development of new alloys [6–12], characterization of their mechanical properties at various temperatures especially at elevated temperatures [4,6,8,13–17], joining technologies [18–22], characterization of physical behaviors including the radiated activation, gas or implantation-driven permeation, electric resistance and magnetic properties [23–31]. Alloying of vanadium and its influence on the mechanical properties is briefly reviewed next.

The mechanical performance of vanadium materials can be varied over a wide range by alloying [1]. In a variety of binary vanadium alloy systems, selected elements such as carbon, tin, boron, copper, zirconium, titanium, tungsten, molybdenum, aluminum, chromium, and nickel change the hardness of vanadium very

* Corresponding author.

0022-3115/99/$ – see front matter
PII: S0022-3115(99)00029-X

remarkably. Most alloy additions improve the strength of the base metal. The addition of a small amount of titanium can also improve the ductility of the vanadium. This is one of the reasons that the ternary alloy system based on vanadium–titanium has significant importance in the development of vanadium alloys. Third-metal additions of chromium, aluminum, and silicon to alloys containing titanium produce a further increase in strength. Furthermore, the forge-ability of the alloys can be maintained. Specifically, titanium and chromium as basic alloying elements can enhance vanadium alloys significantly for practical applications in the field of nuclear power generation. Recent studies have established the priority of using the V–Ti–Cr system as a structural material for tritium breeding blankets and the first wall of fusion reactors [8,32]. Alloying of vanadium with titanium and chromium can trap or lead to localization of nitrogen impurities absorbed from lithium in fine surface layers where it is present in the form of titanium nitride (TiN) [8]. It is evident that the TiN film with dense structure and extremely high inertness is protective and prevents an increase in the rate of metal mass transfer. Experimental studies performed by Evtikhin and Lyublinski [33] reveal that the mass transfer of the V–Ti–Cr alloys by means of lithium flow, containing nitrogen impurity up to 500 ppm, is substantially lower than permissible values. The mechanical properties of such alloys are stable under the simulated lithium circulating conditions. Another advantage of V–Ti–Cr alloy is the decreased weight gain under high temperature water–steam testing conditions. This is due to the formation of the fine passive oxide films such as TiO_2 and Cr_2O_3. These films are highly protective by impeding the process of hydrogen saturation of alloys [34].

Characterization of the mechanical properties of vanadium alloys reveals ductile behavior under monotonic over-loadings at various testing temperatures [4]. The V–Ti–Cr system shows an ideal combination of low room temperature strength and high ductility, high elevated temperature strength and non-heat-treatability [8]. Comparative studies on tensile properties at ambient temperature and elevated temperatures have demonstrated that the percentage of titanium in the binary alloys for optimum strength decreases with increasing temperature. The hot tensile strength of V–Ti alloys can be considerably enhanced by the addition of a third-metal such as chromium or aluminum in low percentage. However, additions of more than 5% of a third metal do not further increase the high temperature tensile strength [1]. Stress–rupture data have been acquired for V–Ti–Cr and V–Ti–Al alloys for further evaluation of the high temperature fracture behavior in the range of 500–700°C. It has been found that the stress–rupture limits are highly temperature dependent, and higher contents of titanium with third metal addition are very useful for increasing the creep strength [1].

The tensile strength of vanadium alloys is also dependent on exposure to radiation. An increase in ultimate tensile strength and yield strength of several alloy systems including V–Ti–Cr alloys have been observed after neutron irradiation at temperatures of 400–700°C, to fluences in the range from 10^{21} to 10^{23} cm^{-2}. The plasticity of all the vanadium alloys was reduced after irradiation. One of the alloys from the V–Ti–Cr family, V–15Ti–7.5 Cr alloy, demonstrated up to 25% increase in yield strength when it was irradiated at 600°C [4]. The tensile properties of V–Ti–Cr ternary alloys are relatively insensitive to the composition over a wide temperature range from 25 to 800°C, though a strengthening effect is observed after irradiation [35]. Nevertheless, high temperature creep rate can be increased upon irradiation [8]. It has also been found that irradiation can cause both low temperature embrittlement and high temperature embrittlement, thus degrading the mechanical properties of vanadium alloys. The low temperature embrittlement occurs in the temperature range lower than 300°C; while high temperature embrittlement appears in the temperature range from 700–1000°C. Titanium is effective in suppressing the low temperature embrittlement, and chromium has the function of alleviating the high temperature embrittlement. Furthermore, the titanium can also reduce the swelling tendency of vanadium alloys during irradiation [20].

The fatigue behavior of vanadium alloys has been studied to a much lesser extent, and data on fatigue crack growth are extremely limited. Comparative studies on the fatigue lifetime of stainless steel and vanadium alloys have been performed [17]. Vanadium alloys of V–Ti–Cr system and V–Cr–Fe–Zr were fatigue tested under various temperature conditions including room temperature, 550°C and 650°C. Both vanadium alloy systems have longer fatigue lifetime than 20% cold-rolled Type 316 stainless steel at elevated temperatures. However, the fatigue property of V–Cr–Fe–Zr alloy system is inferior to that of the V–Ti–Cr alloys, namely V–5Ti–l5Cr at all the three temperatures tested. The fatigue lifetime of unalloyed vanadium at room temperature has been found to change with the hydrogen content [15]. The crack initiation lifetime increases with increasing hydrogen content; while in the propagation range, the lifetime decreases with increasing hydrogen content. It is obvious that the inconsistency in the analysis of the fatigue behavior and the limited database are insufficient for further understanding of the fatigue behavior and assessment of the fracture resistance of vanadium alloys under cyclic loading conditions. It is necessary to acquire fatigue data and study the related fracture and failure mechanisms of promising vanadium alloys, especially from the V–Ti–Cr system.

Stress dominated crack growth behavior has been considered to describe the fatigue crack kinetics of me-

tallic materials under cyclic loading. Classical fatigue crack propagation (FCP) laws express cyclic crack extension in terms of some function of the applied load or stress field in the region near the crack tip. Parameters such as the stress intensity factor, the stress intensity factor range, and the energy release rate are commonly used as correlative tools. Due to its simplicity, the equation proposed by Paris and Erdogan [36] has gained the widest acceptance. In this equation, the crack growth rate is related to the stress intensity factor range, which can be expressed as

$$\frac{da}{dN} = A(\Delta K)^m, \tag{1}$$

where A and m are parameters dependent on material variables, and ΔK is the stress intensity factor range.

The Paris law is valid for describing the commonly observed linearity of the FCP rate within the stable crack propagation region. The inadequacy of this equation to predict FCP rates at both low and high values of the function of the applied load, has led to the development of other fatigue models [37–42].

Strain criteria have also been proposed for describing fatigue crack propagation behavior of metals. Basquin [43] and Manson–Coffin [44,45] proposed the relationships of elastic and plastic strain range versus fatigue lifetime. The total strain range $\Delta\varepsilon_t$ is equal to the sum of elastic strain range, $\Delta\varepsilon_e$, and inelastic strain range, $\Delta\varepsilon_{in}$. That is

$$\Delta\varepsilon_t = \Delta\varepsilon_{in} + \Delta\varepsilon_\epsilon \Rightarrow \Delta\varepsilon_t = B(N_f)^b + C(N_f)^c, \tag{2}$$

where B, C are coefficients of axial elastic and inelastic strain range-life relations, and b, c are exponents of axial elastic and inelastic strain range-life relations.

Any change in materials processing conditions, test conditions, and heterogeneity of the materials mechanical properties lead to the scatter of B, C, b, and c. In most cases, such scatter is not omissible. Therefore, it is not practical to employ these parameters to calculate the fatigue lifetime [46].

In the Palmgren–Miner fatigue lifetime approach [47,48], the corresponding number of cycles to failure, N_f, is applied to compute damage per cycle, D_i, as follows:

$$D_i = \left(\frac{1}{N_f}\right)_i. \tag{3}$$

Damage accumulates in each cycle and failure is considered to occur when the total damage equals unity. However, experimental fatigue tests demonstrate that effective strain increases in such a way that a cycle applied later in testing results in greater damage than a cycle applied earlier [49]. This means the actual damage increases non-linearly which casts doubt on the damage accumulation model of Eq. (3).

All of the above models are based either on analytical methods or semi-empirical approaches. Only the macro-mechanical behavior of materials are considered. It is clear that a comprehensive understanding of fatigue cracking behavior needs observation of the micro-mechanical behavior of materials. The understanding of fatigue cracking through sound principles of fracture mechanics as well as damage formation and evolution during crack advance can provide a more basic rationale for characterizing the resistance of materials to crack propagation.

Recently the modified crack layer (MCL) theory was proposed [50] and its usefulness has been demonstrated to characterize the resistance of various materials to fatigue crack propagation [50–52]. The MCL equation is expressed as [50]

$$\frac{J^*}{a} = \gamma' - \beta'\left[\frac{\dot{W}_i}{a\left(\frac{da}{dN}\right)}\right], \tag{4}$$

where J^* is the energy release rate, a is the crack length, da/dN is the crack speed, $\dot{W}_i$ is the change in work per cycle expended on damage formation and history dependent dissipative processes within the active zone of the propagating crack. The parameters γ' and β' are the specific energy of damage and the coefficient of energy dissipation, respectively. It is the specific energy of damage γ' which has been proven to be a constant, characterizing the resistance of the material to fatigue crack propagation.

In the present work, the fatigue fracture resistance of V–4Ti–4Cr was evaluated using the modified crack layer theory [50]. Analysis of the fracture surface morphology of fatigue tested specimens was also performed to identify the various damage species associated with the different stages of crack propagation kinetics.

2. Material and experimental procedures

The material used in the present work is V–4Ti–4Cr alloy which was received in the form of 1 mm thick rolled sheet. Rectangular specimens with 60 mm length and 12.5 mm width were cut from the sheet. At the center of one free edge of each specimen a 60° V-shaped notch was machined. The radius of the notch tip was about 0.05 mm. The notch depth was about 1.25 mm and the notch depth to sample width ratio (a/w) was kept at 0.1. For static tests, un-notched dog-bone shaped specimens, with 20 mm gage length, were prepared.

Static tensile and fatigue experiments were performed using an 810 materials testing system (MTS) equipped with a 100 kN load cell. The specimens were gripped between two hydraulic wedge grips type 647.10A-01. Static tests based on un-notched specimens were carried

out under displacement control conditions. For fatigue tests, the gage length was 45 mm. All of the fatigue tests were conducted at ambient temperature of 25°C under load control conditions using a frequency of 3 Hz. The maximum stress was 130 MPa, and the ratio of minimum stress to maximum stress was 0.1. A sinusoidally varying stress was used. The crack length at various intervals of number of cycles was recorded during the tests. A video camera connected to a WV-5470 video monitor was used to view the crack tip region to measure the crack length and capture the damage associated with the crack growth. A total of three samples were tested and a typical sample was used for both the fatigue crack propagation analysis and the fracture surface examination.

The fracture surface was cut away from selected static and fatigue failed specimens and soaked in acetone with ultrasonic vibration for half an hour to remove any contaminants. The specimens were dried in high speed flowing inert gas. Then the specimens were fixed on a cylindrical sample holder using electrically conductive adhesive. The fracture surfaces were examined using a Hitachi S-2150 scanning electron microscope operated at a maximum acceleration voltage of 25 kV. The micrographs were recorded on Polaroid 55 instant films and the images were transmitted simultaneously into a microcomputer equipped with Quartz PCI Version 3.01 image processing software. The images can be also printed out.

3. Results and discussion

In this work, the results are presented and discussed under four main sections: static overload behavior, fatigue crack growth data, fatigue resistance parameters, and fatigue fracture surface morphology. It should be mentioned that the data reported here are from a typical sample chosen from three fatigue specimens and that the scatter in the data is less than 5%.

3.1. Static overload behavior

A typical stress–strain curve of the V–4Ti–4Cr is shown in Fig. 1. The stress is calculated based on the original cross-sectional area of the specimen before testing. In the strain range up to 1.5%, the relationship between stress and strain is linear. The calculated Young's modulus is about 13.5 GPa. In the strain range from 1.5% to 5%, the stress–strain relationship is nonlinear. This range corresponds to the initial yielding of the alloy. The yielding strength reaches about 280 MPa. Following this range, strain hardening can be observed, corresponding to the strain range of 5–9.5%. The material reached its ultimate strength of 420 MPa at about

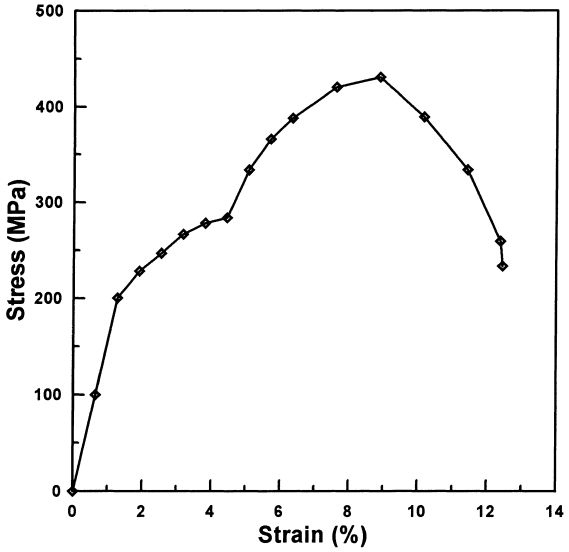

Fig. 1. Stress–strain relationship of V–4Ti–4Cr.

9.5% strain, then the tensile strength dropped down and the specimen broke at about 220 MPa. The strain to failure is about 12.5% approximately.

The fracture surface of the V–4Ti–4Cr after static testing was examined using scanning electron microscopy. The whole fracture surface is considerably rough as seen in Fig. 2. Severe cavitation with dimples in various sizes, are observed. Such features are indicative of ductile fracture mechanisms associated with the overloading tensile tests. This cavitation and void coalescence appears to be the mechanism of fracture of V–4Ti–4Cr alloy under tension overloading.

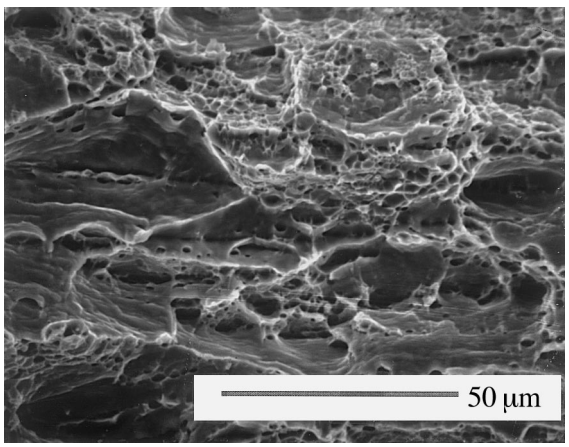

Fig. 2. Micrograph showing the fracture features of V–4Ti–4Cr with a lot of cavitation sites and multi-geometrical dimples under monotonic static tensile loading.

3.2. Fatigue crack growth data

3.2.1. Fatigue lifetime

As mentioned previously in the experimental procedure section, the fatigue crack length was measured using a video camera system, from the edges of the notched crack at various intervals of number of fatigue cycles. Nearly 100 times magnification can be obtained from this monitoring and display system. A plot of the crack propagation length, a, versus the number of cycles, N, for the V–4Ti–4Cr under consideration is shown in Fig. 3. From the results shown in Fig. 3, it can be seen that the total fatigue lifetime of the vanadium alloy is approximately 1 050 000 cycles; and there exists a very big difference in magnitude between the initiation lifetime and the propagation lifetime. The initiation lifetime reaches 800 000 cycles, and it takes most of the total fatigue lifetime. The crack length increases from the initial 1.25 mm to about 1.55 mm. The propagation lifetime is about 250 000 cycles. The crack length grows in a stable manner up to about 10.0 mm. The crack moves very fast in the last several thousand cycles, and the critical crack length reaches approximately 11.15 mm.

3.2.2. Crack growth rate

The slope of the curve in Fig. 3 is taken as the average crack growth rate (da/dN) at each crack length. The relationship between, da/dN, and crack length, a, is shown in Fig. 4. The log of the values of da/dN are plotted for convenience. The curve illustrated in this figure demonstrates a crack growth kinetics of a sigmoidal feature, which means that the FCP kinetics can be divided into three stages. The first stage is the crack initiation or the threshold. In the second stage, a crack deceleration is observed, due to the damage formation and microstructural evolution in the vicinity of the crack tip. This will be discussed later in the section regarding the fracture surface examination. The curve approached asymptotic values in the third stage (critical stage). In all the three stages; crack initiation, crack deceleration and the critical stage, the crack growth rate for the vanadium alloy varied appreciably. The crack growth rate in the initiation stage for the V–4Ti–4Cr sample ranges between 1×10^{-10} to 5×10^{-9} m/cycle. The crack growth rate in the second stage ranges from 5×10^{9} m/cycle to 4×10^{-7} m/cycle. The last stage exhibits a crack growth rate larger than 4×10^{-7} m/cycle. The crack growth rate, at each crack length or at the corresponding number of cycles, will be employed in the analysis of this alloy using the MCL theory.

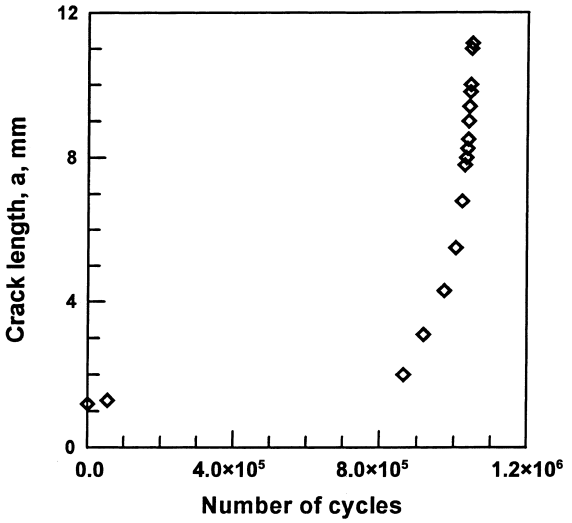

Fig. 3. Crack length versus the number of cycles for the V–4Ti–4Cr alloy.

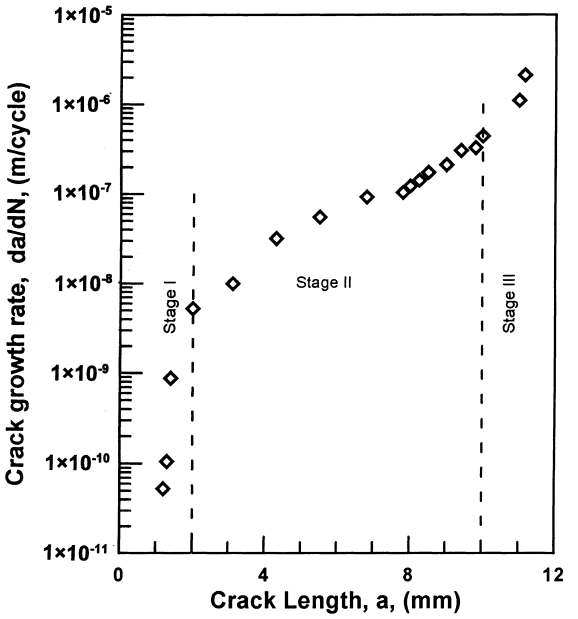

Fig. 4. The crack growth rate, da/dN, versus crack length, a for the V–4Ti–4Cr alloy.

3.2.3. Energy release rate

The potential energy, P, was calculated from the loading and un-loading curves recorded at intervals of number of cycles as the area above the unloading curve. On this basis, the relationship between the potential energy, P, and the fatigue crack length, a, was established. The energy release rate was obtained from the potential energy versus crack length relationship as

$$J^* = \frac{1}{B}\left(\frac{\partial P}{\partial a}\right), \tag{5}$$

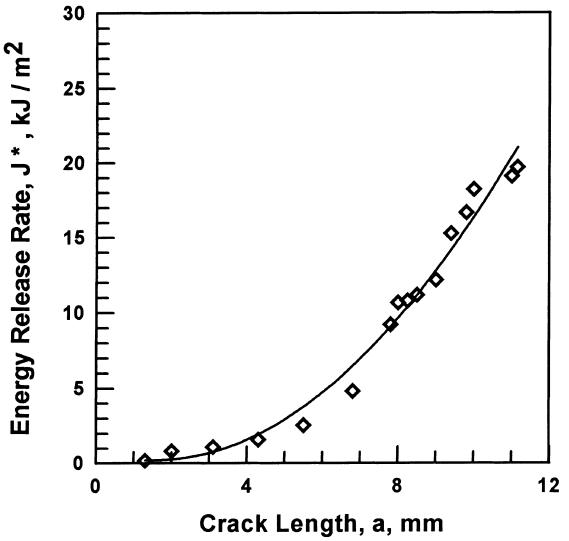

Fig. 5. The energy release rate, J^*, versus crack length, a, for the V–4Ti–4Cr alloy.

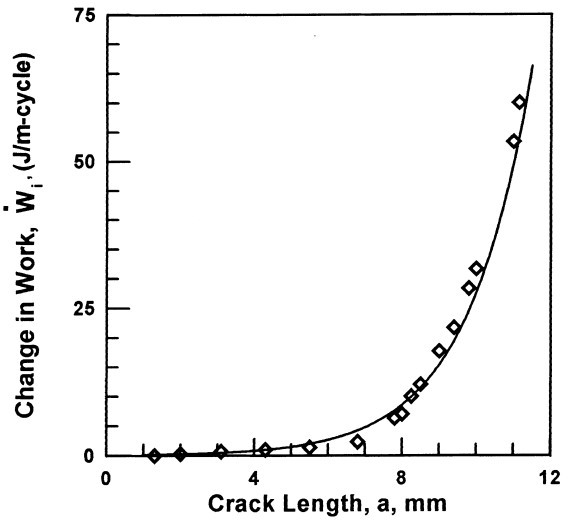

Fig. 6. Change in work, $\dot{W}_i$, versus the fatigue crack length, a, for the V–4Ti–4Cr alloy.

where B is the specimen thickness, P is the potential energy, a is the crack length.

The energy release rate, J^*, is shown in Fig. 5 as a function of the crack length, a, for the V–4Ti–4Cr material. Again, the values of J^* at different crack lengths will be used for the determination of γ' and β' using the MCL theory.

3.2.4. The change in work

In this study, the hysteresis loops were recorded at intervals of crack length. The hysteresis energy as represented by the area of each loop, was measured using a planimeter. The hysteresis energy was then used for the determination of the change in work per cycle, $\dot{W}_i$ as follows:

$$\dot{W}_i = \frac{1}{B}(H_i - H_o), \tag{6}$$

again B is the specimen thickness, H_i is the area of hysteresis loop at a crack length (a_i) and H_0 is the area of hysteresis loop before crack initiation (a_o).

The relationship between the change in work, $\dot{W}_i$, and the crack length, a, for the V–4Ti–4Cr material is shown in Fig. 6. As it can be seen in Fig. 6, the value of $\dot{W}_i$ reaches about 5 J/m · cycle at a crack length of 7 mm. Fast increase in $\dot{W}_i$, is observed at crack lengths greater than 8 mm. Thus, the V–4Ti–4Cr material consumes more energy for damage formation towards the second stage of FCP. The relationship between $\dot{W}_i$ and a will be used in the MCL model to extract the fatigue fracture parameters γ' and β'.

3.2.5. Fatigue resistance parameters

The parameters γ' and β' have been evaluated using the MCL theory along with the experimental data previously calculated: a, da/dN, J^*, and $\dot{W}_i$. If the experimental results are in accordance with the MCL model equation 14, a plot of J^*/a versus $\dot{W}_i/[a(\mathrm{d}a/\mathrm{d}N)]$ should give a straight line. Indeed, based on the results presented in Fig. 7, a straight line is obtained for the V–4Ti–4Cr, with γ' being the intercept of the line and β' being the slope. This attests to the applicability of the

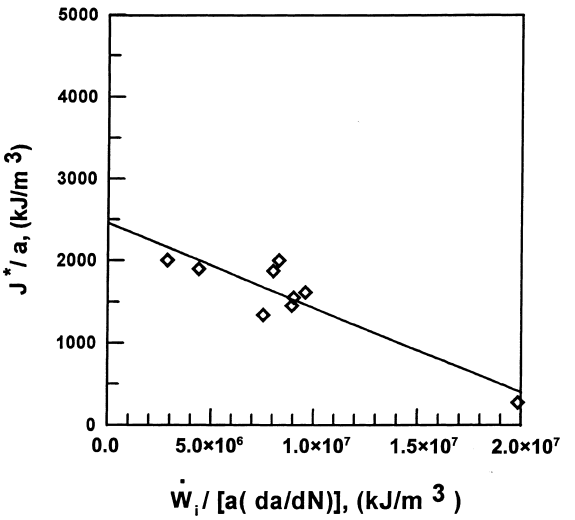

Fig. 7. Fatigue crack propagation data for the V–4Ti–4Cr specimens to obtain γ' and β' using the MCL theory.

MCL model to describe the FCP behavior of the V–4Ti–4Cr material. The values of γ', and β' for the vanadium alloy were found to be 2500 kJ/m^3 and 10.3×10^{-5}, respectively. A higher value of γ' indicates higher resistance to FCP since more energy is required to cause a unit volume of the material to change from an undamaged state to a damaged state.

Unlike the energy release rate J^*, the specific energy of damage γ', is independent of the geometry of the specimens. As expressed in the MCL theory of Eq. (4), J^* and γ' are closely related to each other, with a complementary term comprising β'. On one hand, the energy release rate serves as the crack driving force. On the other hand, γ' can be considered as a material property related parameter, effectively reflecting the fatigue fracture toughness or the resistance of the V–4Ti–4Cr alloy to FCP. Unalloyed vanadium has a relatively closed packed refractory body centered cubic (BCC) structure [53,54]. When alloy elements such as titanium and chromium were introduced, a single phased structure with the added element in the substitutional positions in vanadium crystal formed. To some extent, the regular stacking state of the vanadium material may be interrupted due to the difference in atomic size between vanadium and alloy elements. Thus cross grid of dislocations can form in the initial stage of deformation as happens in other refractory alloy systems [55,56], leading to considerably high lattice frictional stress by the substitutional elements such as Ti and Cr. This can explain the strengthening effect of the two alloying elements. On the other hand, the twinning and slip deformation of the BCC crystalline structure can be kept as long as the alloying element content is in a reasonable range [57]. All of these processes related to deformation and crack growth are large consumers of energy. Thus, the value of the specific energy of damage, γ', is expected to be high. Also, the critical value of the energy release rate of the V–4Ti–4Cr is considerably high as can be seen from Fig. 3. Consequently, the material demonstrates ductile fracture behavior, which will be further discussed in the section regarding the analysis of fracture surface morphology.

The fatigue crack growth rate versus the energy release rate for the V–4Ti–4Cr alloy based on the experimental data is shown in Fig. 8. It can be seen from Fig. 8 that the relationship between da/dN and J^* follows the familiar S-shaped curve. Unlike other fatigue models, the MCL model proved to be capable of describing such behavior. This indicates that the modified crack layer model closely describes fatigue crack propagation behavior over the entire range of the crack driving force with a more practical methodology from the engineering view point. The curve displays the familiar S-shaped behavior, indicating three stages of FCP. A threshold stage is followed by a stage of decreased acceleration and then a stage of unstable crack

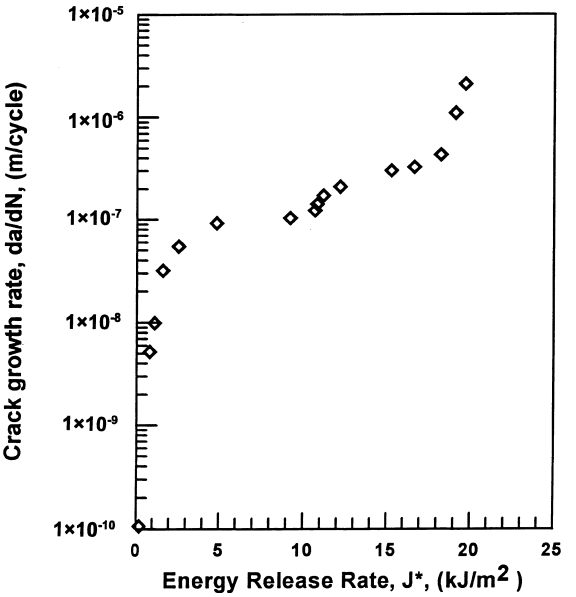

Fig. 8. The crack growth rate (da/dN) versus the energy release rate, J^*, for the V–4Ti–4Cr.

propagation. This is indicative of material damage within the area in front of the crack tip associated with fatigue crack propagation, which has been previously investigated for other kinds of materials [58]. Interestingly, this analysis of the fatigue crack propagation kinetics is basically in agreement with the calculated results of crack speed, da/dN, versus crack length, a as shown in Fig. 4.

3.2.6. Fatigue fracture surface morphology

The fracture surface for a typical specimen of V–4Ti–4Cr, failed under fatigue loading, is schematically shown in Fig. 9. The notch is at the left hand side of the sample. The crack propagated from left to right. The fracture surface can be divided into three distinct regions according to the morphological features. Region I corre-

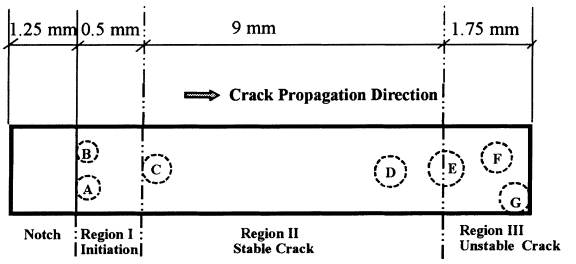

Fig. 9. Schematic representation of the fatigue fracture surface showing the fatigue regions and location of micrographs for further analysis.

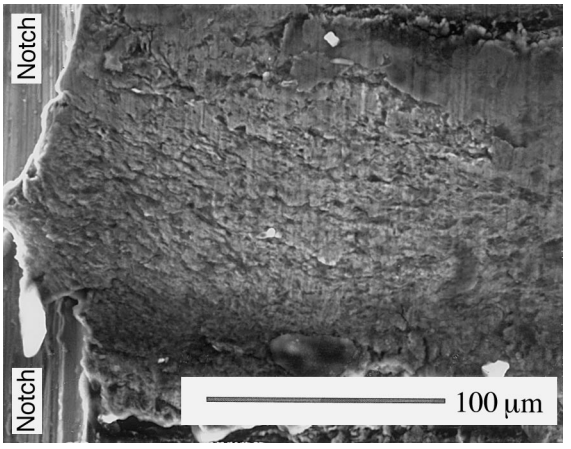

Fig. 10. SEM micrograph of the first region, showing a large piece of damaged material.

sponds to crack initiation or the threshold stage. Region II represents stable crack propagation, and Region III corresponds to the unstable or critical crack stage. The first region is around 0.5 mm in length and contains the global fracture features associated with the threshold crack propagation. Immediately ahead of the notch tip exists severe plastic deformation indicated by the darker tongue like features. This plastic deformation created extrusions and intrusions on the fracture surface. The micrograph of Fig. 10 was taken at point A in Fig. 9. This location, A, contains the extrusion surface caused by the plastic deformation. The plastic flow is clear in Fig. 10 which caused the material to flow over part of the notch surface as seen on left side of the micrograph. Also Fig. 10 displays discontinuities in the form of micro-voids and micro-cracks in addition to fatigue striations. The micrograph in Fig. 11 was taken from the intrusion area, location B in Fig. 9. A combination of voids, secondary micro-cracks and striations can be seen in Fig. 11. In some particular areas, the material was broken and separated into several parts. The splitting may also occur along the grain boundary of the V–4Ti–4Cr.

The second region is the stable crack propagation region which is about 9 mm in length. This region contains the main fracture surface features responsible for crack deceleration as shown in Fig. 4, da/dN versus a. At the beginning of this second region, point C in Fig. 9, corresponds to the onset of crack deceleration.

Considerable rough fracture features can be seen in this region. Such features are generally formed due to void growth and coalescence [59]. Extensive plastic deformation associated with the crack growth is found. Drawn-out peaks in very elongated 'necks' indicate large deformation before final separation. The formation of micro-cracks and micro-voids are also found as shown in Fig. 12, a micrograph taken at location C. Extensive micro-cracks aligned perpendicular to the fatigue crack propagation direction indicate the inhomogeneous deformation in micro-domains during the growth of the main crack. Some of the micro-cracks are irregular in shape and connected with each other into a web-like pattern, demonstrating the inter-crystalline void or crack formation by fatigue damage. Another micrograph taken from the crack deceleration zone, further down from location C, shows fatigue striations as depicted in Fig. 13. Formation of numerous micro-cracks and inter-crystalline separation can also be seen in Fig. 13. All of these fracture surface features reflect severe fatigue damage and indicate a high energy consuming process associated with the crack propagation, in this region.

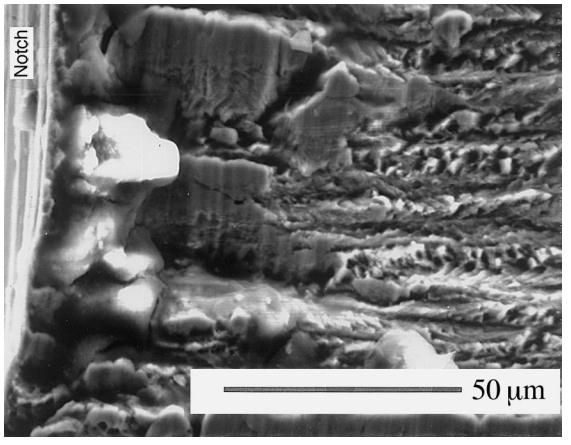

Fig. 11. SEM micrograph showing the voided are a and broken grains of the V–4Ti–4Cr alloy.

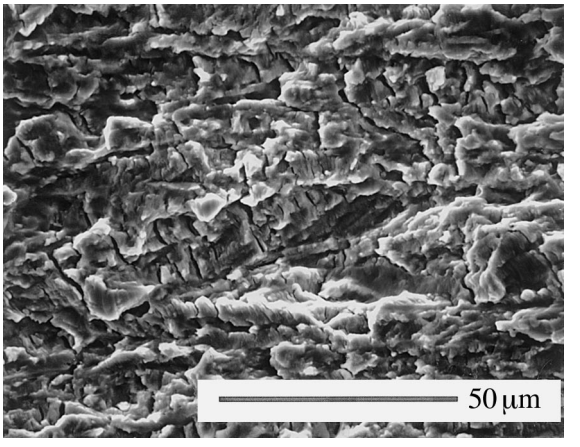

Fig. 12. SEM micrograph of the second region, showing the micro-cracks and inter-granular voids resulted from severe fatigue damage.

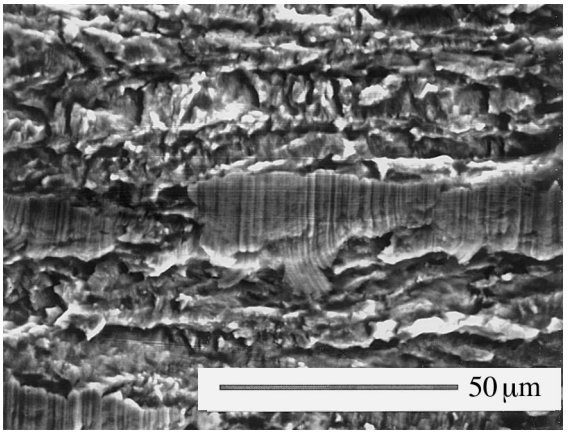

Fig. 13. SEM micrograph of the second region, showing the fatigue striations, also revealing the micro-cracks and inter-granular voids due to severe fatigue damage.

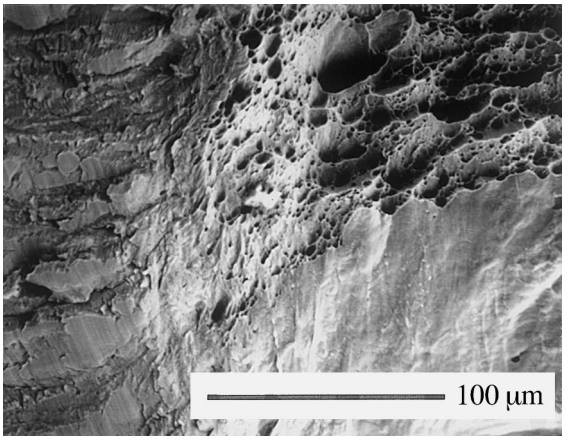

Fig. 15. SEM micrograph showing the transition from the second region to the third region.

Location D in Fig. 9 represents the end of the second stage of crack propagation kinetics shown in Figs. 4 and 8. Fatigue striations, secondary cracks, cavitation or micro-voids can be found in the acceleration zone as shown in Fig. 14. However, the fracture surface of this zone is smoother than that at location C. The number of micro-cracks or micro-voids is much fewer than that observed at the beginning of the stable crack region (location C). Obviously, the consumed energy related to the fatigue crack growth in this location is less than that in location C. This can be the explanation of the increase in crack growth rate at the end of the stable crack propagation stage.

The unstable crack propagation region, shown in Fig. 9, is about 1.75 mm in length. This region is characterized by fast or critical crack propagation features. Very large deformation was observed during crack growth. Like in the static tensile process, the material undergoes significant deformation. The transition from the second region to the third region, location E in Fig. 9, is shown in Fig. 15. The left part of this micrograph represents the end of the stable crack region which contains striations, and some micro-cracks as previously found at location D in Fig. 9. The right part of Fig. 15 illustrates the beginning of the unstable crack propagation region. Dimples of various size are clearly seen in the upper right corner indicating ductile fracture mechanisms. The lower right part of the micrograph, Fig. 15, shows a shear lip due to the fully developed plane stress condition [60]. In this region, the

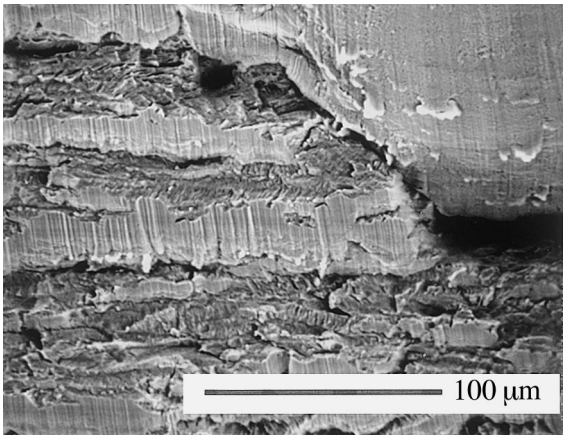

Fig. 14. SEM micrograph showing another view of the second region near the third region. The fracture surface is very smooth revealing less energy consuming in FCP. Fatigue striations, micro-cracks and inter-granular voids can be also found.

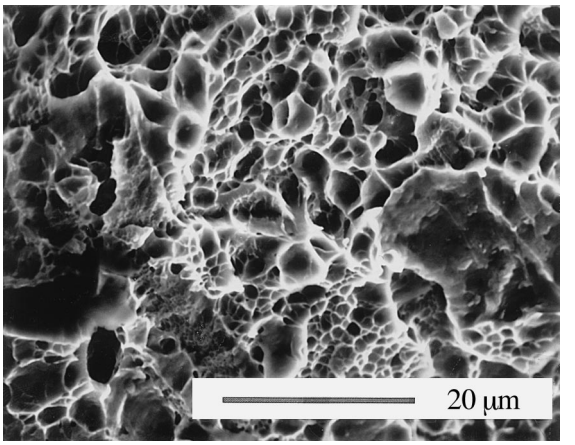

Fig. 16. SEM micrograph of the third region, showing tensile dimples in equiaxied shape. Inter-granular voids can be also found.

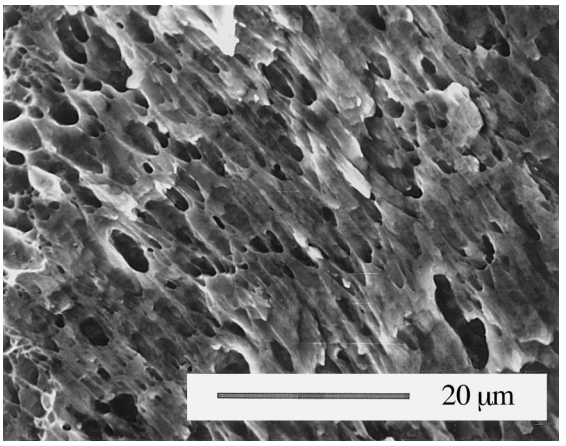

Fig. 17. SEM micrograph of the third region, showing shear dimples in oval and parabolic shapes related to the shear deformation in the shear lip zone.

main crack grows at an angle and a single shear lip is formed.

Fig. 16 shows dimples of fairly uniform size generated under tensile stress; location F in Fig. 9. Some of these dimples are very shallow, while others are considerably deep. Also shown in this micrograph are micro-voids along grain boundaries, indicating the intergranular separation in the final stage of the fatigue crack propagation. Shear dimples [61] are shown in Fig. 17; location G in Fig. 9. Elongated dimples in oval shape or parabolic shape reveal the shear deformation of the V–4Ti–4Cr alloy in this zone. All of these fracture surface features associated with the last region demonstrate a ductile fracture mechanism.

4. Conclusions

The static tensile behavior of the V–4Ti–4Cr is characterized by large plasticity and ductile fracture mechanism as manifested in cavitations and void coalescence on the fracture surface. The yield strength of the material is approximately 280 MPa, and the ultimate tensile strength is 420 MPa. The strain to failure is 12%.

Fatigue crack propagation (FCP) kinetics of this vanadium alloy displayed the familiar S-shape da/dN versus a curve. Three distinct stages can be clearly observed, a threshold stage followed by a stage of reduced acceleration, indicative of crack tip damage, and then a stage of critical (unstable) crack propagation.

The MCL theory appears to be capable of describing the FCP behavior of the V–4Ti–4Cr alloy. The value of the specific energy of damage, γ', proposed as a material parameter characterizing the resistance of the V–4Ti–4Cr alloy, was found to be about 2500 kJ/m^3. The coefficient of dissipation, β', was found to be 7.8×10^{-5}.

Analysis of the fatigue fracture surface morphology reveals different features corresponding to the three FCP stages. Cavitation and micro-void coalescence are dominant in the first region related to the accelerated cracking in the threshold stage. The fracture surface in the second region shows numerous micro-cracks, voids, drawn-out material and striations indicating fatigue damage evolution and high energy consumption during FCP. The third fracture region which is associated with the fast or critical crack propagation stage exhibits two zones of extensive deformation; a zone with tensile overload dimples of different sizes and a shear lip zone with elongated voids or shear dimples in the crack propagation direction.

Acknowledgements

The authors acknowledge the support of the US Department of Energy (DOE) under contract number DE-FG02-96ER54384. Tyron Harper, an undergraduate student at Tuskegee University, is acknowledged for the preparation of the test specimens.

References

[1] W. Rostoker, The Metallurgy of Vanadium, Wiley, New York, 1958, p. 139.
[2] C.G. Johnson, W.R. Weeks, Metallurgy, 4th ed., American Technical Society, Chicago, 1957, p. 147.
[3] F.A. Cotton, G. Wilkinson, Advanced Inorganic Chemistry, 5th ed., Wiley, New York, 1998, pp. 666–667.
[4] D.L. Smith, B.A. Loomis, D.R. Diercks, J. Nucl. Mater. 135 (1985) 125.
[5] A.B. McIntosh, K.Q. Bagley, J. Inst. Met. 84 (1956) 251.
[6] D.R. Diercks, B.A. Loomis, J. Nucl. Mater. 141–143 (1986) 1117.
[7] W.R. Johnson, J.P. Smith, K. Richardson, Adv. Mater. Proc. 151 (6) (1997) 25.
[8] S.N. Votinov, M.I. Solonin, Y.I. Kazennov, V.P. Kondratjev, A.D. Nikulin, V.N. Tebus, E.O. Adamov, S.E. Bougaenko, Y.S. Strebkov, A.V. Sidorenkov, V.B. Ivanov, V.A. Kazakov, V.A. Evtikhin, I.E. Lyublinski, V.M. Trojanov, A.E. Rusanov, V.M. Chernov, G.A. Birgevoj, J. Nucl. Mater. 233–237 (1996) 370.
[9] J.R. Peterson, D.B. Smathers, J. Nucl. Mater. 141–143 (1986) 1113.
[10] O.N. Carlson, F.A. Schmidt, Evolution of Refractory Metals and Alloys, 1994, pp. 1.
[11] C.K. Gupta, Int. Met. Rev. 29 (1984) 405.
[12] H.U. Borgstedt, M. Grundmann, J. Konys, Z. Peric, J. Nucl. Mater. 155 (1998) 690.
[13] O.A. Medvedev, A.I. Ryazanov, A.N. Lyubimov, Y.V. Tichonov, W. Vanwitzenburg, J. Nucl. Mater. 233–237 (1996) 460.
[14] T. Shibayama, I. Yamagata, H. Kurishita, H. Kayano, J. Nucl. Mater. 239 (1996) 162.

[15] D.L. Harrod, R.E. Gold, Int. Met. Rev. 25 (1980) 163.
[16] K. Kainuma, N. Iwao, T. Suzuki, R. Watanabe, J. Less-Common Met. 86 (1982) 263.
[17] K.C. Liu, J. Nucl. Mater. 103&104 (1981) 913.
[18] A. Sunwoo, Scripta Mater. 37 (1997) 691.
[19] R.F. Mattas, B.A. Loomis, D.L. Smith, J. Miner. Met. Mater. Soc. 44 (8) (1992) 26.
[20] B.A. Loomis, D.L. Smith, J. Nucl. Mat. 191 (1992) 84.
[21] N.B. Potluri, M.L. Grossbeck, H. Aglan, B.A. Chin, 'Investigation on embrittlement of V–4Cr–4Ti alloy during fusion welding', Presented on the Conference of Trends in Welding '98, to be published in the ASM Proceedings, 1998.
[22] H.T. Lin, D.N. Braski, J. Nucl. Mater. 217 (1994) 209.
[23] E.T. Cheng, J. Nucl. Mater. 239 (1996) 1467.
[24] M.E. Elzain, A.A. Yousif, Hyperfine Interact. 94 (1-4) (1994) 1879.
[25] S.M.L. Galdino, C.C. Dantas, R. Vangrieken, Anal. Chim. Acta 196 (1987) 337.
[26] H. Kawanishi, S. Ishino, E. Kuramoto, J. Nucl. Mater. 143 (1986) 899.
[27] A.C. Klein, D.K. Sze, J. Nucl. Mater. 49 (1987) 261.
[28] B. Stolecki, A. Borodziukkulpa, W. Zahorowski, J. Mater. Sci. 22 (8) (1987) 2933.
[29] D.F. Holland, R.A. Anderl, Fusion Tech. 14 (2) (1988) 707.
[30] R. Jayaram, M.K. Miller, Scripta Metall. Mater. 27 (1) (1992) 77.
[31] O.G. Romanenko, I.L. Tazhibaeva, V.P. Snestakov, A.K. Klepikov, Y.V. Chikhray, A.V. Golossanov, B.N. Kolbasov, J. Nucl. Mater. 237 (1996) 376.
[32] D.L. Smith, H.M. Chung, B.A. Loomis, H.C. Tsai, J. Nucl. Mater. 233–237 (1996) 356.
[33] V.A. Evtikhin, I.E. Lyublinski, J. Adv. Mater. 1 (1994) 60.
[34] A.I. Dedyurin, L.I. Gomozov, S.N. Votinov, J. Phys. Chem. 5 (1983) 22.
[35] H. Bohm, Nucl. Metall 18 (1973) 163.
[36] P. Paris, F. Erdogan, Trans. ASAFE, (Dec.) 1963, 528.
[37] R.G. Forman, V.E. Kearney, R.M. Engle, J. Basic Eng. 89 (1967) 459.
[38] S. Pearson, Eng. Fract. Mech. 4 (1972) 9.
[39] B. Mukhergeo, D.J. Burns, J. Exp. Mech. 11 (1971) 433.
[40] S. Arad, J.C. Radon, L.E. Culver, J. Mech. Eng. Sci. 13 (1971) 75.
[41] J.C. Radon, S. Arad, L.E. Culver, Eng. Fract. Mech 6 (1974) 195.
[42] C.A.M. Branco, J.C. Radon, L.E. Culver, J. Test Eval. 3 (1975) 195.
[43] O.H. Basquin, The exponential law of endurance tests, Proceedings, American Society for Testings and Materials, West Conshohocken, PA, 10, 1910, pp. 625–630.
[44] S.S. Manson, Behaviors of Materials under Conditions of Thermal Stress, Proceedings, Heat Transfer Symposium, University of Michigan Research Institute, 1953, pp. 9–75.
[45] L.F. Coffin Jr., A study of effects of cyclic thermal stress on a ductile metal, Am. Soc. Mech. Eng. Trans. 76 (1954) 931.
[46] V. Kliman, P. Fuleky, J. Jelemenska, Residual Operating Fatigue Lifetime Estimation of Distribution Function, Advances in Fatigue Lifetime Predictive Techniques (Third Conference), ASTM STP 1292, American Society for Testing and Materials, West Conshohocken, PA, 1996, pp. 305–327.
[47] H.O. Fuchs, R.I. Stephens, Metal Fatigue in Engineering, Wiley, New York, NY, 1980.
[48] J.A. Bannantine, J.J. Comer, J.H. Handrock, Fundamentals of Metal Fatigue Analysis, Prentice Hall, Englewood Cliffs, NJ, 1990.
[49] S.W. Tipton, Multiaxial plasticity and fatigue life prediction in coiled tubing, Advances in Fatigue Lifetime Predictive Techniques (Third Conference), ASTM STP 1292, American Society for Testing and Materials, West Conshohocken, PA, 1996, pp. 283–304.
[50] H. Aglan, Int. J. Damage Mech. 2 (1993) 53.
[51] H. Aglan, A. Othman, L. Figueroa, J. Mater. Sci. 29 (1994) 4786.
[52] H. Aglan, Z. Abdo, J. Adhes. Sci. Technol. 10 (1996) 183.
[53] K. Wang, R. Reeber, Mater. Sci. Eng. R23 (1998) 101.
[54] S. Diplas, P. Tsakiropoulos, R.M.D. Brydson, J.F. Watts, Mater. Sci. Tech. 14 (1998) 699.
[55] K. Jagannadham, F.C. Laabs, J. Mater. Sci. 22 (1987) 803.
[56] K. Jagannadham, F.C. Laabs, J. Mater. Sci. 22 (1987) 818.
[57] K. Jagannadham, J. Mater. Sci. 22 (1987) 4251.
[58] H. Aglan, A. Moet, Int. J. Fract. 40 (1989) 285.
[59] T.L. Anderson, Fracture Mechanics, CRC, Boca Raton, FL, 1991, p. 305.
[60] D. Broek, Elementary, Engineering Fracture Mechanics, Martinus Nijhoff, Dordrecht, 1987, p. 269.
[61] C.R. Brooks, A. Choudhury, Metallurgical Failure Analysis, McGraw-Hill, New York, 1993, p. 144.